

Fast electron propagation in high density plasmas created by shock wave compression

J J Santos¹, D Batani², P McKenna³, S D Baton⁴, F Dorchies¹,
A Dubrouil¹, C Fourment¹, S Hulin¹, Ph Nicolaï¹, M Veltcheva²,
P Carpeggiani², M N Quinn³, E Brambrink⁴, M Koenig⁴,
M Rabec Le Glohaec⁴, Ch Spindloe⁵ and M Tolley⁵

¹ CELIA, Université Bordeaux 1-CNRS-CEA, Talence, France

² Dipartimento di Fisica 'G. Occhialini', Univ. degli Studi di Milano-Bicocca, Milan, Italy

³ SUPA, Department of Physics, University of Strathclyde, Glasgow, UK

⁴ LULI, Ecole Polytechnique - CNRS - CEA, Palaiseau, France

⁵ Rutherford Appleton Laboratory, Chilton, Didcot, UK

Received 1 August 2008, in final form 11 September 2008

Published 9 December 2008

Online at stacks.iop.org/PPCF/51/014005

Abstract

We present one of the first results of relativistic laser intensities of the transport of fast electrons in high density and warm plasmas. The fast electrons are produced by the interaction of 40 J, 1 ps, $5 \times 10^{19} \text{ W cm}^{-2}$ laser pulses with solid foil targets. A 200 J, 1.5 ns laser focalized over a 500 μm diameter zone on the opposite side of the foil is used to create a shock propagating through and compressing the target to 2–3 times its solid density before the relativistic interaction. For both the solid and the compressed cases, the fast electron transport divergence and range are investigated, via the $K\alpha$ emission from an embedded copper layer, for a conducting (aluminium) and an insulating (plastic) target material.

(Some figures in this article are in colour only in the electronic version)

1. Introduction

It is clear that the fast ignitor approach to inertial fusion [1] concerns the propagation and energy deposition of a fast electron beam in strongly compressed materials, i.e. the pellet of nuclear fuel and the dense hot plasma surrounding it.

To date, most of the experimental results on fast electron generation and transport have been obtained in solid density targets. An exception to this has been an experiment performed at the Rutherford Appleton Laboratory, 10 years ago, with laser pulses delivering maximum intensities of $10^{17} \text{ W cm}^{-2}$ [2]. That experiment showed a much larger fast electron penetration in the shocked material (about a 100% increase), which was due to the phase change produced in the target material by the shock wave. While the initially cold solid target was an insulator (plastic), the shocked target was ionized and changed to a conductor state by shock compression

and heating. Theoretical and numerical analyses showed how the effects of self-generated strong electric fields were essential for the interpretation of the results [3].

More recently, an experiment on fast electron transport in cylindrically compressed targets has been done at Osaka University [4]. A 10–20% efficiency was estimated for the coupling between an intense laser ($\sim 10^{19}$ W cm $^{-2}$) and a 200 eV, 6–9 g cm $^{-3}$ imploded plasma column of 30 μ m diameter. Numerical work reproducing the experiment put in evidence the fast electrons radial confinement over a depth of 300 μ m by self-generated magnetic and electrostatic fields. This explained the efficient heating of the hot and dense plasma column.

As in Hall's experiment [2], in this paper we also present results on fast electrons propagation and energy deposition in high density plasmas created by planar shock wave compression, but these are the first to be obtained at laser intensities $> 10^{19}$ W cm $^{-2}$, relevant to fast ignition. In spite of the lower density and temperature regime obtained when compared with a cylindrical or spherical compression, the planar compression geometry assures the target is homogeneous around the fast electrons propagation axis. This way, all the fast electrons cross identical regions and the interpretation of the different mechanisms ruling their propagation can be more easily understood. Besides the comparison between solid and shocked material, we have also tested the effects of the initial conductivity of the targets (conductor/dielectric), using either aluminium (Al) or plastic (CH) for the propagation layer.

2. Experimental setup and interaction conditions

The results were obtained at the PICO 2000 laser system at LULI, coupling a 200 J, 1.5 ns compression beam with a counter-propagating CPA 40 J, 1 ps high-intensity beam. To produce a uniform compression of the material, the ns beam was focused to a flattop 500 μ m diameter spot using a random phase plate. The ns beam was converted to $2\omega_0$ in order to reduce preheating while maximizing shock pressure, and also to ease alignment (while keeping a different wavelength with respect to the ps beam). Focusing the ps beam to 10–13 μ m diameter spots produced intensities on a target of $(3\text{--}5) \times 10^{19}$ W cm $^{-2}$, capable of generating intense currents of fast electrons through the in-depth regions of the target, shock-compressed to 2–3 times the initial solid density. In reality, due to technical constraints in the interaction chamber, the two beams were not exactly counter-propagating, the ns laser beam being focused at 45° on the target *rear* side, while the ps beam was focused at 22.5° on the target *front* side. This does not imply any change in the basic scheme because both the generated shock and the fast electron beam are travelling normally to the target. The scheme of the experiment is shown in figure 1.

The diagnostic system was based on incorporating at the rear of the targets a fluorescent bi-layer made of 10 μ m Cu and 10 μ m Al. The K α signal from the Cu layer was recorded using a spherical Bragg crystal, which imaged the x-ray source [5] onto image plates. This imaging diagnostic enabled measurement of 2D images with a 10.8 magnification of the spatial distribution of fast electrons as they cross the Cu tracer (producing ionization followed by K α emission). This allowed reconstruction of the fast electron beam geometry and divergence. The K α emission from the Al layer was recorded in the 1st diffraction order by a conical crystal x-ray spectrometer [6]. Its spectral resolution of 1.7 eV enabled measurement of both the K α from cold Al atoms and the shifted K α emission from Al ions. Since the degree of ionization in the Al layer is a function of temperature, in principle such a diagnostic can infer the background temperature in the tracer by measuring the ratio between cold and *hot* K α lines [7]. The spectrometer also measured the Cu K α emission in the 5th diffraction order. Both diagnostics enabled measurement of the propagation range of fast electrons in the material by plotting the K α signal versus target thickness obtained on different shots.

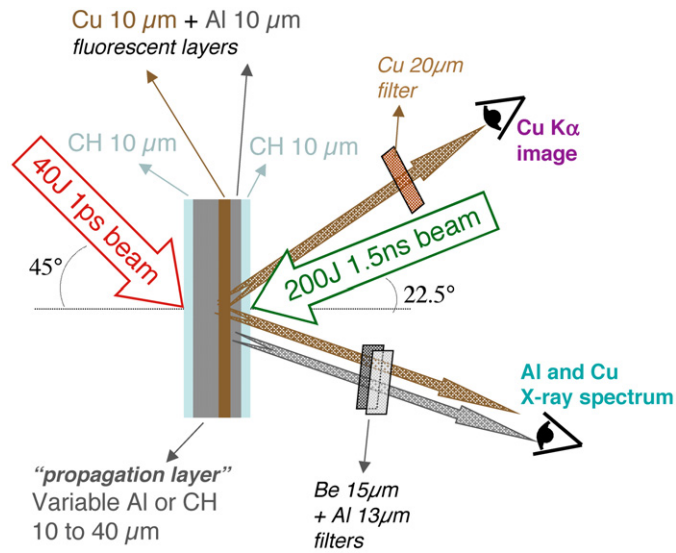


Figure 1. In-principle scheme of the experimental setup and of the targets.

The thickness to be changed was the *propagation layer* (as shown in figure 1). We used both *conducting* targets (Al propagation layer) and *insulating* target (plastic layer) in order to compare different materials, which have shown different propagation characteristics in previous works [8, 9], and to see if they behave in a similar way under shock compression. For each kind of target, the results are compared with the cold case (no compression beam).

In the case of the Al layer, the Cu layer also filtered the x-ray emission from the propagation layer, so that only the Al x-rays emitted from the Al tracer layer could reach the spectrometer. An additional plastic layer, of 10 μm thickness, was added on both sides of the target. On the ns side this served to reduce preheating which could arise from the direct interaction of the ns beam with Al. The presence of plastic on the ps beam was due to the fact that in all cases we wanted the same fast electron source; therefore we chose to have the laser always interacting with a plastic layer. At the same time, plastic reduced any x-ray preheating, which could arise due to the laser's prepulses. Finally, a very thin Al layer was added onto the plastics in order to avoid laser shine-through.

2.1. Timing of the ps/ns beams

The first part of the experiment was devoted to the characterization of the shock wave produced by the ns laser beam, in particular its velocity, both as a means of characterizing the material parameters through the equation of state, and as a way to find the right synchronization between the ns and the ps beams (this last must be fired before shock breakout in order to assure that no plasma is produced on the ps side, so that the interaction always takes place with a cold solid surface and the mechanism of hot electron production is not varied).

For different targets, the breakout times were measured by a time-resolved imaging of the *front* side using a streak camera. Some of the results, using the same sweep speed, are shown in figure 2: the left image was obtained by directly imaging the ns laser pulse (no target) into the streak camera, giving the reference time t_0 for the arrival of the ns pulse onto the target *rear* side. The shock breakout time is reproduced by 1D MULTI hydrodynamic simulations for the

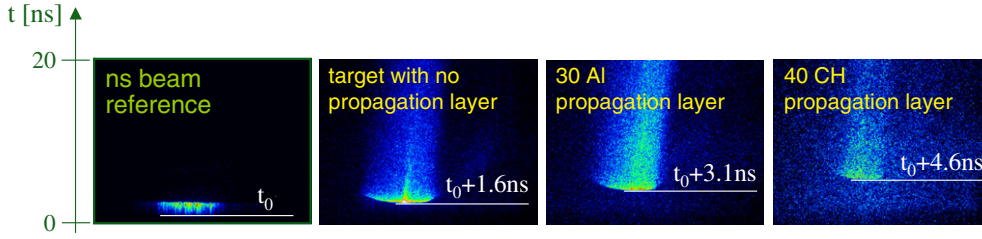


Figure 2. Time-resolved images of the ns beam induced shock breakout emission from the *front* side of the targets. The image on the left is a direct image of the laser pulse.

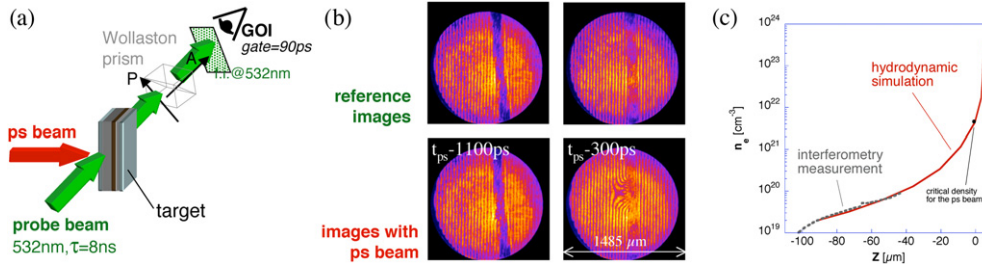


Figure 3. (a) Transverse interferometry setup. (b) Interferometric images of the targets without the CPA laser beam (reference images) and with the CPA beam at different times before the intense part. (c) Comparison between the measured (dashed grey curve) and the calculated (solid red curve) pre-plasma density profile (the dot indicates the critical density position for the CPA beam).

different targets. Accounting for the shock propagation velocity on the different materials and coupling the simulations to the streak measurements, the ps/ns laser pulses delay was chosen for each kind of target according to its propagation layer material and thickness in order to leave the last $10 \mu\text{m}$ of plastic (on the ps side) uncompressed.

2.2. Target hydrodynamics

To correctly understand the x-ray results and to properly model the fast electron generation and transport through the targets, we need to know their exact state (density and temperature profiles) when the ps beam interacts. For that, besides the ns-induced shock, we must also consider the effects of the ps beam ASE pedestal. Fast diode measurements show a 2×10^{-3} energy contrast. The pedestal corresponds to a ramp whose FWHM duration of 1.1 ns has been precisely characterized by interferometry of the pre-plasma formed on the *front* side of the target, using a 8 ns, ~ 10 mJ, 532 nm Quanta-Ray probe beam across the target surface and a Wollaston prism between two crossed linear polarizers (see figure 3(a)). With regular steps for the triggering of the 90 ps gated optical imager (GOI) used as detector, we obtained interferometric snapshots of the target at different times relative to the ps beam (see figure 3(b)). Reference images were systematically acquired before every shot, enabling a reference for the initial target front side position. The *genesis* of the pre-plasma was detected to happen 1100 ps before the intense pulse arrival.

The phase shift along a chord through the medium is deduced from the shift position of the fringes of the interferograms. Assuming a cylindrical symmetry for the pre-plasma around the target normal, using Abel inversion, we deduce the radial distribution of the refractive

index, and therefore of the electron density n_e . A pre-plasma expanding to $\approx 100 \mu\text{m}$ is measured $250 \pm 45 \text{ ps}$ before the intense part of the pulse arrival.

While the ns beam induced shocks are reproduced by 1D hydrodynamics, the ps beam small spot size implies a 2D hydrodynamical behaviour. We used the 2D hydrodynamic code CHIC to account for both the ns beam and the ASE-pedestal perturbations. For what concerns the ASE effects, we see in figure 3(c), showing the electron density profiles normal to the target surface on the centre of the interaction region, the simulations match the interferometry measurements in the range 10^{19} – 10^{20} cm^{-3} . The black dot indicates the critical density $n_c = 4.56 \times 10^{21} \text{ cm}^{-3}$ for the $1.06 \mu\text{m}$ ps laser pulse (accounting for the relativistic correction of the electron mass). The critical density surface has moved from its initial position, $Z = 0$, by less than $1 \mu\text{m}$.

Besides creating the pre-plasma, fundamentally from the ablation of the front CH layer, with consequences to the ps laser coupling with matter (density gradient length, displacement of the critical surface) and therefore to the fast electron generation, the ASE pedestal also produces non-negligible effects on the propagation and fluorescent layers. This can be seen in figure 4 showing the density profiles of different targets for both *solid* (ps beam only) and *compressed* (ps + ns beams) cases. A first effect is the ASE induced shock propagating left to right at $z = 10 \mu\text{m}$ depth and compressing the beginning of the propagation layer to $\sim 4 \text{ g cm}^{-3}$ over $1 \mu\text{m}$ for the Al case, and to $\sim 2 \text{ g cm}^{-3}$ over $5 \mu\text{m}$ for the CH case. This is not so important, but one also sees that the *front* side CH layer is almost completely ablated by the ASE pedestal and therefore the total overdense thickness of the target is reduced by roughly $10 \mu\text{m}$. Because of this, in the case of the ns + ps interaction, we can also realize that against our predictions from the streak measurements and the preliminary 1D hydrodynamic simulations accounting only for the ns laser beam, some of the targets have already expanded due to the ns-shock breakout (e.g. targets with $10 \mu\text{m}$ Al and $40 \mu\text{m}$ CH propagation layers; cf figure 4). This situation can affect the interpretation of the x-ray results (presented further below), as the *front* side density profile (scale gradient and critical density position) is not the same for the two situations, and thus probably neither the generated fast electron populations. The influence of laser coupling to the pre-plasma on the fast electron jet initial divergence and on its energy content and distribution are currently being investigated by PIC simulations.

3. Fast electron transport results

Plots (a) and (b) in figure 5 show typical x-ray spectra obtained with the conical-crystal spectrometer, for dielectric and conductor $10 \mu\text{m}$ propagation layer targets. On each panel we compare the solid (ps beam only) and compressed (ns + ps beams) target cases. For the solid case, we could only detect the Cu $K\alpha$ lines. For the compressed case they were initially masked by the $\sim 500 \text{ eV}$ ns-Al plasma He- α emission, which we could eliminate by using an additional $13 \mu\text{m}$ Al filter on the spectrometer. The Al $K\alpha$ lines, which we label on the Al-ns + ps spectrum, were almost never detected in this experiment, which rules out the possibility of measuring the target rear side temperature upon the fast electrons energy deposition. The Cu $K\alpha$ spectral lines integrated emissions are compiled in figure 5(c) as a function of the overdense thickness between the critical density position on the ps laser side till the middle of the Cu-fluorescent layer. We see the signal yields are lower for the compressed targets for both the Al and the CH propagation layers. Without compression, signals are stronger for Al (open black symbols) than for CH (open red symbols) targets. With compression, signal yields for the Al (full black symbols) and for the CH (full red symbols) targets are comparable. These observations are confirmed by the 2D images of Cu $K\alpha$ emission yields.

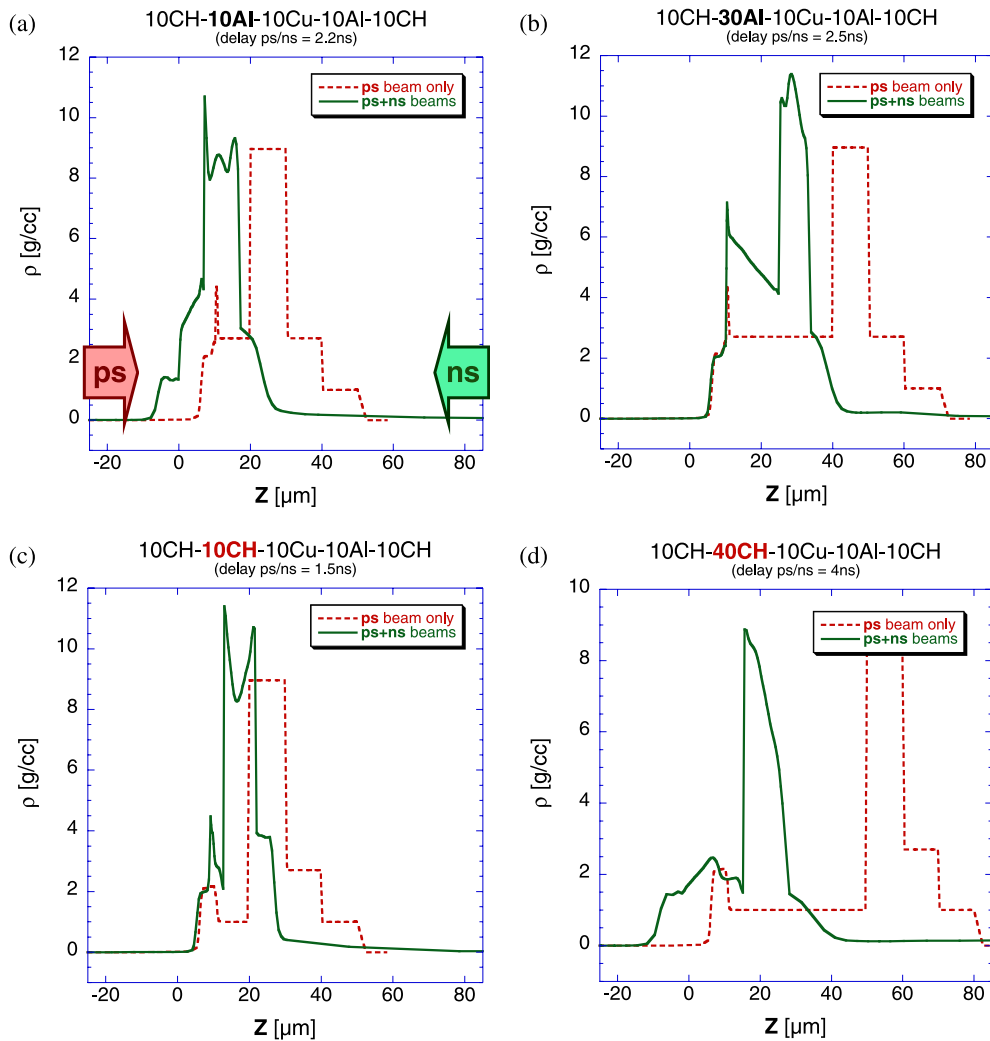


Figure 4. CHIC 2D hydrodynamic simulations of the different experimental situations: symmetry axis density profiles at the intense ps pulse arrival moment for targets with propagation layers of: (a) 10 μm Al, (b) 30 μm Al, (c) 10 μm CH and (d) 40 μm CH. Red dashed curves correspond to the *solid* case and solid green curves to the *compressed* case. The directions of the ps and ns beams are indicated in plot (a).

Figure 6 shows typical images of the Cu $K\alpha$ emission, obtained with the spherical Bragg crystal, for different thicknesses of the CH propagation layer. The graph on the right shows the Cu $K\alpha$ signal radius evolution against the overdense thickness between the critical density position on the ps laser side till the middle of the Cu-fluorescent layer. We see that there is no significant difference on the fast electron jet divergence while it propagates through solid or compressed matter. The half-angle divergence can be roughly evaluated to $\sim 50^\circ$, which is rather large.

In principle, for the used planar geometry, shock compression does not significantly change the stopping power of matter due to collisions: the atomic parameters of the target material temperature appear inside a logarithmic term and therefore do not produce large variations.

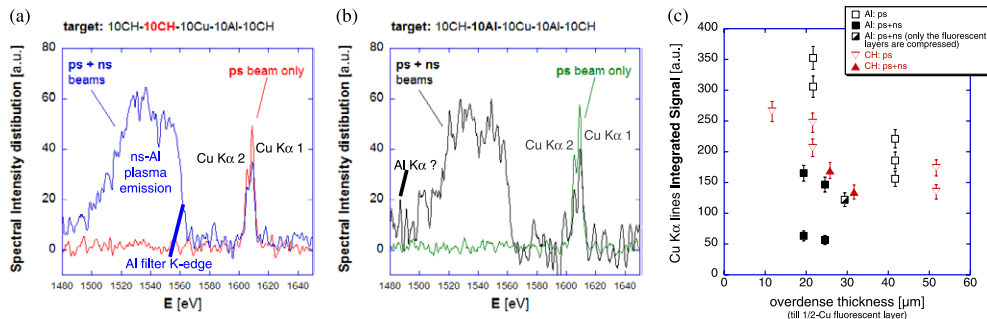


Figure 5. Typical x-ray spectra: solid versus shock compressed targets for (a) dielectric and (b) conductor propagation layers. (c) Resumed Cu $K\alpha$ spectral lines integrated emission against the overdense thickness between the critical density position on the ps laser side till the middle of the Cu-fluorescent layer.

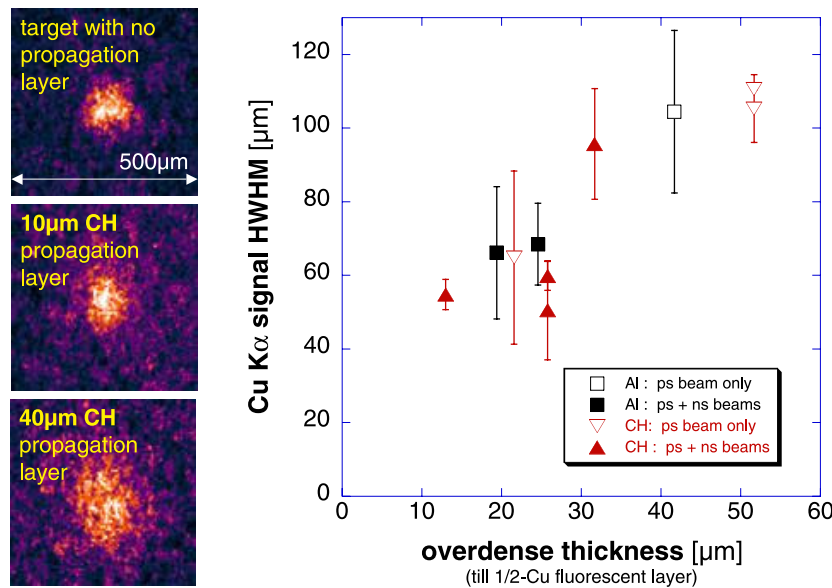


Figure 6. Typical Cu $K\alpha$ signal images for ns + ps shots on targets of variable CH propagation layer thickness. The graph on the right shows the spot radius (HWHM) as a function of the overdense thickness till the middle of the Cu layer.

The collisional stopping power is instead proportional to the target density (appearing outside of the logarithmic term) which is directly and strongly affected by shock compression (up to a maximum factor of 4 for strong single shocks, in theory). However, since a 1D compression up to a certain factor reduces the target thickness of the same factor, for a given initial target the total areal density remains the same and no large variations of the collisional stopping power are expected from the compression.

To test the role of the collisions and/or collective effects on the fast electrons stopping power, we plot in figure 7 the same set of results as a function of the areal density ρZ . For each target, this parameter was integrated from the axis density profiles calculated by the 2D hydrodynamic code, between the critical density and the middle of the Cu layer. Figure 7(b)

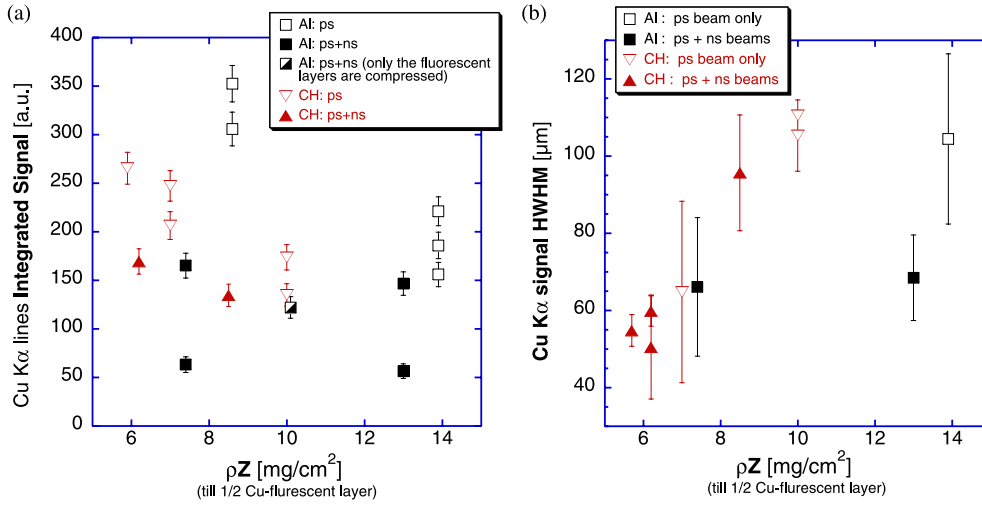


Figure 7. (a) Cu $K\alpha$ spectral lines integrated emission and (b) Cu $K\alpha$ spot radius (HWHM) against the target areal density.

shows the Cu $K\alpha$ signal radius evolution against the target's areal density. *A contrario* of the scaling against the overdense thickness (cf figure 6), a collimated propagation seems to happen on compressed Al layers (full black symbols). No such behaviour is deduced either for compressed CH layers or for solid layers (conductor or insulator).

The comparison of the Cu $K\alpha$ fluorescence against ρZ between the Al and the CH targets, or between the solid or the compressed targets, (figure 7(a)) approximately shows the same scaling as against the targets overdense thickness (cf figure 5(c)), but the data from the compressed targets (full symbols) is pretty constant against ρZ (within shot to shot fluctuations) and independent of the propagation layer material. This may mean that collisions do not play a preponderant role on the fast electrons stopping power.

Hence, any remarkable difference between the detected fluorescence levels for the solid and the compressed cases should in principle be ascribed to an *anomalous* stopping of the fast electrons associated with collective transport mechanisms (due to self-generated magnetic fields and self-generated electric fields) and/or to fluorescence and opacity variations of the rear tracer layers. Collective effects should be dramatically affected by compression of the targets both because of the change in the material properties and because, for instance, the deceleration of hot electrons in the electric field is proportional to $\int \vec{E} \cdot d\vec{l}$ and therefore to the total target thickness, which is reduced in the compressed case. According to this, one would expect to obtain higher fluorescence yields for the compressed targets, which is not what we have measured (cf figure 5(c)).

An extra point is plotted in figures 5(c) and 7(a) (black half-filled square) corresponding to a $20\ \mu\text{m}$ propagation layer target where the ps laser beam was timed to arrive when only the rear CH and the fluorescent layers have been compressed by the ns beam (delay ps/ns = 2 ns), leaving the propagation and front CH layers still uncompressed. The fluorescent yield detected for this test is comparable to the yields obtained for the compressed propagation layers. This indicates that we probably must consider the higher Cu $K\alpha$ reabsorption by the hot and compressed plasma behind the fluorescent layer (*rear* side of the target): it would explain the decrease of the detected signal for the compressed case relative to the solid case.

4. Conclusions

We have presented results for fast electron transport in shock compressed foil targets obtained for the first time at laser intensities relevant for fast ignition ($> 10^{19} \text{ W cm}^{-2}$). A complete physical picture of the observed phenomena is not available for the moment. Our results still need to be checked by careful modelling and simulations accounting for both hydrodynamics and fast electron transport and induced heating. For each target layer, we must consider density and temperature-dependent properties: the collisional stopping power (bound and free electrons + plasmons), the Cu K shell ionization cross section, the electrical conductivity, the electric field transport inhibition and the role of magnetic fields.

Based only on the fluorescence yields of a target-embedded copper layer, we can nevertheless point out a few preliminary conclusions. As already observed in previous works [8], in solid matter the fast electron transport is more inhibited in CH layers (insulator) due to electric field effects. The fast electron penetration range is equivalent for compressed CH and Al, as both layers are partially ionized and behave like a conducting plasma independently of their initial nature.

Comparing the solid and the compressed cases, the number of detected Cu $K\alpha$ photons is less in the last case, but we still have to compute the x-rays reabsorption on the *rear* solid or plasma layers to get the real emission yields. We will then be able to conclude on the number of electrons reaching the Cu layer and to properly discuss the fast electron transport efficiency in high density plasmas compared with solid density targets.

Acknowledgments

The authors gratefully acknowledge the staff at LULI 2000 (the laser and the experimental area teams, and the design engineer) for their enormous help before and during the experiment. They also wish to express their gratitude to J R Davies, K Lancaster, P Norreys and R Scott for the beam time of their campaign used to complete the data sets of this paper. Support from EPSRC and COST P14 is gratefully acknowledged.

References

- [1] Tabak M *et al* 1994 *Phys. Plasmas* **1** 1626
- [2] Hall T A *et al* 1998 *Phys. Rev. Lett.* **81** 1003
- [3] Batani D *et al* 2000 *Phys. Rev. E* **61** 5725
- [4] Nakamura H *et al* 2008 *Phys. Rev. Lett.* **100** 165001
- [5] Stephens R B *et al* 2004 *Phys. Rev. E* **69** 066414
- [6] Martinolli E *et al* 2004 *Rev. Sci. Instrum.* **75** 2024
- [7] Martinolli E *et al* 2006 *Phys. Rev. E* **73** 046402
- [8] Pisani F *et al* 2000 *Phys. Rev. E* **62** R5927
- [9] Manclossi M *et al* 2006 *Phys. Rev. Lett.* **96** 125002